

# Asteroseismology of GD358 with complex C/O core profiles

Agnés Bischoff-Kim<sup>1</sup>, J. L. Provencal<sup>2,3</sup>, M. H. Montgomery<sup>3,4</sup>, Samuel T. Harrold<sup>4</sup>, B. Howard<sup>3</sup>, W. Strickland<sup>5</sup>, D. Chandler<sup>5</sup>, D. Campbell<sup>5</sup>, A. Arredondo<sup>5</sup>, R. Linn<sup>5</sup>, D. P. Russell<sup>5</sup>, D. Doyle<sup>5</sup>, A. Brickhouse<sup>5</sup>, R. Linn<sup>5</sup>, D. Peters<sup>5</sup>, A. V. Kusakin<sup>6</sup>, A. V. Sergeev<sup>7</sup>, M. Andreev<sup>7</sup>, A. Maksim<sup>7</sup>, S. Velichko<sup>7</sup>, R. Janulis<sup>8</sup>, F. Aliçavuş<sup>9</sup>, N. Horoz<sup>9</sup>, S. Zola<sup>10,11</sup>, W. Ogłóza<sup>10,11</sup>, D. Koziel-Wierzbowska<sup>10,11</sup>, T. Kundera<sup>10,11</sup>, D. Jableka<sup>10,11</sup>, B. Debski<sup>10,11</sup>, S. Meingast<sup>12</sup>,

## ABSTRACT

We report on .....

*Subject headings:* Stars: oscillations — Stars: variables: general — white dwarfs

## 1. Astrophysical Context

White dwarfs are the end product of evolution for around 98% of the stars in our Galaxy. Buried in their interiors are the records of physical processes that take place during earlier

---

<sup>1</sup>Penn State Worthington Scranton, Dunmore, PA 18512; axk55@psu.edu

<sup>2</sup>University of Delaware, Department of Physics and Astronomy Newark, DE 19716; jlp@udel.edu

<sup>3</sup>Delaware Asteroseismic Research Center, Mt. Cuba Observatory, Greenville, DE 19807

<sup>4</sup>Department of Astronomy, University of Texas, Austin, TX 78712; mikemon@rocky.as.utexas.edu

<sup>5</sup>Meyer Observatory and Central Texas Astronomical Society, 209 Paintbrush, Waco, TX 76705; chandler@vvm.com

<sup>6</sup>Fesenkov Astrophysical Institute, Almaty 050020, Kazakhstan

<sup>7</sup>Ukrainian National Academy of Sciences, Main Astronomical Observatory, Golosiiv, Kiev 022 252650; sergeev@terskol.com

<sup>8</sup>Institute of Theoretical Physics and Astronomy, Vilnius University, Vilnius, Lithuania; jr@itpa.lt

<sup>9</sup>Ulupinar Observatory, Çanakkale Onsekiz Mart University, Turkey

<sup>10</sup>Astronomical Observatory of the Jagiellonian University, ul. Orla 171, 30-244 Cracow, Poland; szola@oa.uj.edu.pl

<sup>11</sup>Mount Suhora Observatory, Cracow Pedagogical University, Ul. Podchorazych 2, 30-084 Krakow, Poland; zola@astro1.as.ap.krakow.pl

<sup>12</sup>Institut für Astrophysik, Universität Wien, Türkenschanzstrasse 17, 1180 Wien, Austria

stages in the life of the star. Nuclear reaction rates during the core helium burning phase set the core composition of white dwarfs, while the relative time spent burning hydrogen and helium during the asymptotic-giant-branch (AGB) phase and mass-loss episodes determine the thickness of the helium layer (??). Helium atmosphere white dwarfs (DBs) comprise roughly 20% of the population of field white dwarfs, with most of the remaining 80% consisting of their hydrogen atmosphere (DA) cousins. The bifurcation into two spectral classes is thought to occur during post-AGB evolution when, in some cases, a very late thermal pulse burns off the residual hydrogen in the envelope, producing a nearly pure helium atmosphere (?). Such objects are then supposed to return to the white dwarf cooling track as PG 1159 stars, which are widely believed to be the precursors of most DB white dwarfs. DBs are found to pulsate at effective temperatures ranging between 21,000 K and 28,000 K (??).

The subject of this paper, GD358 (V777 Her) is the brightest ( $m_v = 13.7$ ) and best studied helium atmosphere white dwarf pulsator. It is located near the red edge of the instability strip ( $T_{\text{eff}} =$ ,  $\log g =$ ). GD358’s pulsation spectrum contains a series of independent modes, many with complex multiplet structure. Models involving magnetic fields have been proposed to explain that structure (?). Of importance for this work is the fact that the spacing of the multiplets is consistent with theoretical predictions for a series of  $l = 1$  modes (?).

Paradoxically, among the DBVs that have enough detected periods to be fitted asteroseismically, GD358 is the only one that has not been analyzed using the complex C/O profiles adapted and parameterized from stellar evolution calculations ([e.g.]??). The most recent fits of GD358 (?) were performed using 11 observed modes and simple models where the oxygen abundance drops linearly from its central value to zero.

Pulsating white dwarfs do not pulsate in all their available modes at all times. We have maintained an active observing program of this complex star in an effort to identify additional frequencies. These new observations have identified additional periods in GD358’s pulsation spectrum, bringing the total known modes to 15. Thirteen of these modes belong to a consecutive  $\ell = 1$  sequence, the longest sequence observed in a DBV. This sequence is critical to constrain the asteroseismic fits and better define the limitations of high precision white dwarf asteroseismology.

We present a new detailed asteroseismic analysis of GD358, taking advantage of its long sequence of  $\ell = 1$  modes to better constrain the asteroseismic fits and define the limits of high precision white dwarf asteroseismology. Our goals are two-fold. First, we will incorporate advanced asteroseismic models to explore parameter space ?. For example, the even period spacing observed in GD358’s pulsation spectrum is consistent with the theory of g-mode non-radial pulsations. The magnitude of the spacing is expected to be related to how compressible

the stellar interior is. The compressibility of the interior should be inversely proportional to the effective temperature. A hotter object would be less compact. On the other hand, a more massive model will have a higher density and be less compressible. These properties lead to distinguishable features of the models in the mass versus effective temperature parameter plane. We can explore such features with GD358 because we have a long, confirmed, single  $\ell$  sequence of modes of higher radial order.

Secondly, the present analysis allows us to place GD358 in the context of stellar evolution. According to the models, the precursors of DBs emerge from the born-again phase with envelopes containing a nearly uniform mixture of helium (He), carbon (C), and oxygen (O) out to the photosphere (??). As the PG 1159 stars cool, the helium diffuses upward and gradually accumulates to form a chemically pure surface layer. Through the DBV instability strip, this process is still ongoing so that instead of a pure helium layer surrounding the carbon and oxygen core, one has a region where the carbon and helium are still mixed. This leads to a double layered structure, with the pure He surface layer overlying the remainder of the uniform He/C/O envelope, all above the degenerate C/O core. A key prediction of the diffusion models is that, for a given stellar mass, the pure He surface layer will steadily grow thicker as the DB star cools. GD358 is the fourth DBV we can use to check this theory. The other three DBVs (???) have painted a picture consistent with the diffusion calculations, with the hotter best fit models having thinner pure helium layers. With GD358, we seek to confirm this trend qualitatively.

In Section 2, we present our new observations and outline the data reduction process. In Section 3, we establish the framework for frequency identification, and present the list of frequencies used for the asteroseismic investigation. Section ?? outlines the asteroseismic investigation, and .....

## 2. New Observations and Data Reduction

GD358 was discovered in 1982 (?) and has been the target of the Whole Earth Telescope (WET) in 1990, 1994, 2000, and 2006 (???). New observations presented here include 254 individual observing runs (1105.1 hrs) spanning 2007-2015 (Table ??). Each season of observations was obtained as part of multisite WET campaigns.

Standard procedure for WET observations calls for observers to transfer raw images and calibration files to WET headquarters for analysis at the end of each local night. CCD data reduction follows the steps described in ?. In brief, the new observations were obtained with different CCD photometers, each with distinct effective bandpasses. We minimize the

bandpass issues by using CCDs with similar detectors whenever possible and employing a red cutoff filter (BG40 or S8612) to normalize wavelength response and reduce extinction effects. We corrected each image for bias and thermal noise, and normalized by the flat field. Aperture photometry using the Maestro photometry pipeline described by ? was performed on each image, utilizing a range of aperture sizes for the target and comparison stars. For each individual nightly run, we chose the combination of aperture size and comparison star(s) producing the highest signal/noise light curve.

We used the WQED pipeline ? to examine each nightly light curve for photometric quality, remove outlying points, divide by suitable comparison stars, and correct for differential extinction. Our observational technique is therefore not sensitive to oscillations longer than a few hours. The result is a series of light curves with amplitude variations represented as fractional intensity (mmi). The unit is a linear representation of the fractional intensity of modulation ( $1 \text{ mmi} \approx 1 \text{ mmag}$ ). We present our Fourier transforms (FTs) in units of modulation amplitude ( $1 \sim \text{mma} = 1 \times 10^{-3} \text{ ma} = 0.1\% = 1 \sim \text{ppt}$ ).

The final reduction step is to combine the individual light curves (Figure 1) to produce complete light curves for GD358 for each observing season. We assume GD358 oscillates about a mean light level. This assumption allows us to carefully assess overlapping segments from different telescopes and identify and correct any vertical offsets. As discussed in detail in ?, we find no significant differences between the noise levels of amplitude spectra using: 1) the combination of all light curves including overlapping segments from different telescopes, 2) the combination of light curves where we retain only higher signal to noise observations in overlapping segments and 3) combining all light curves using data weighted by telescope aperture.

The result is a series of new light curves for each observing season between 2007 and 2015. 2007 contains 8.1 hrs of observation, 2008 26.1 hrs, 2009 45 hrs, 2010 201.3 hrs, 2011 401.1 hrs, 2012 150.5 hrs, 2013 87 hrs, 2014 184.6 hrs, and 2015 55 hrs. Our coverage is not complete, and this incompleteness produces spectral leakage in the amplitude spectra. To quantify this, we sampled single sinusoids using exactly the same times as the original data for each season. The resulting amplitude spectrum, or “spectral window”, is the pattern produced in the FT by a single frequency. The FTs for 2010, 2011, and 2014 are given in Fig. 2.

### 3. Frequency Identification

Our goal is to compile a complete list of GD358’s observed independent and combination frequencies to be used in a comprehensive asteroseismic analysis. GD358 is known for large scale changes in amplitudes and small but not insignificant frequency variations on a variety of timescales (?). The amplitude and frequency variations evident in Fig. 2 will produce artifacts in FTs, greatly complicating any frequency analysis. We reanalyzed all available archival data (????) as well as our new observations to insure continuity in methodology. We use *Period04* (?) for Fourier analysis and nonlinear least squares fitting to select statistically significant peaks in each FT. As discussed in ?, we adopt the criterion that a peak must have an amplitude at least four times greater than the average noise level in the given frequency range. We define “noise” as the frequency-dependent average amplitude after prewhitening by the dominant frequencies. This is a conservative estimate, as it is impossible to ensure that all of the “real” frequencies are removed when determining the noise level. This is certainly true for GD358, where the peaks above  $\approx 2500 \mu\text{Hz}$  are combination frequencies (?). Fig. 3 displays the average noise as a function of frequency for the 2007-2015 observing seasons. A similar plot for the archival data is presented in Figure 3 of ?. To confirm our uncertainty estimates, we calculated Monte Carlo simulations using the routine provided in *Period04*. This routine generates a set of light curves using the original times, the fitted frequencies and amplitudes, and added Gaussian noise. A least squares fit is performed on each simulated light curve, with the distribution of fit parameters giving the uncertainties. Our Monte Carlo results are consistent with our average noise estimates.

Our frequency selection procedure involves identifying the largest amplitude resolved peak in the FT, fitting a sinusoid at that frequency to the data set, subtracting the fit from the light curve, recomputing the FT, examining the residuals, and repeating the process until no significant power remains. This technique, known as prewhitening, must be employed with an over-abundance of caution, especially since we are aware of amplitude and/or frequency modulation in our data set. A detailed discussion of the prewhitening procedure and steps taken to minimize the effects of amplitude modulation is given in (?). Our final identifications of independent frequencies detected in each observing season are given in Table ?? and Table ??.

## 4. Frequency Analysis

### 4.1. Frequencies Distribution

Perusal of Tables ?? and ?? shows that GD358’s observed frequencies vary in two important ways. First, frequencies detected in a given observing season are not found in all observing seasons. Asteroseismology is based on the assumption that the available pulsation frequencies are linked to stellar structure. Since we are fairly certain that GD358’s internal structure does not change on the timescales of the observations, we can assume that GD358 excites different subsets of its available pulsations at different times. While this is a common phenomenon seen in white dwarf pulsators, the selection mechanism remains mysterious. The best way to determine GD358’s complete set of pulsation frequencies is to combine frequency identifications from multiple observing seasons as outlined in (?).

Figure 4 presents a schematic representation of GD358’s pulsation frequencies for all the available data. The features of asteroseismic importance are the localized bands between 900 and 2400  $\mu\text{Hz}$  (1100 and 400 s). We interpret each band to represent a single radial overtone in GD358. The bands themselves illustrate the second way in which GD358’s frequencies vary. Each band consists of frequency detections from multiple observing seasons, but each band is significantly wider in frequency space than the frequency error of any single measurement, arguing that some process is acting on the frequencies. The simplest explanation is rotational splitting. However, with the exception of the two highest frequency (shortest period) bands ( $k = 8$  and  $k = 9$  from ?), we find no clear evidence of multiplet structure in the frequency distributions of the lower frequency (longer period) bands. The lower frequency band widths are most likely the result of amplitude and/or frequency modulation that obscures any underlying signatures of rotational splitting.

Figure 4 also shows that the widths of the bands is not constant, but changes from band to band. ? presents an interesting analysis of the hydrogen atmosphere pulsator (DAV) kic 4552982, in which they identify 17 bands of pulsation frequencies. This DAV follows the general pattern exhibited by GD358: the highest frequency (shortest period) mode shows evidence of rotational splitting, while the lower frequency (longer period) modes are complex bands. The authors note that this DAV’s bands have different widths in frequency space, and that there may be astronomical significance to this. Although the observational timebases are quite different (20 months for kic 4552982 vs 30 years for GD358), our data presents the opportunity to investigate this for a DB pulsator. We measured the width of each of GD358’s band. We define ”width” as the difference between the lowest and highest frequency detected in each band. Figure 6 presents the results. The widths of GD358’s bands are commensurate with those found in kic 4552982. We also find a general increase in width with decreasing

frequency (increasing period), until we reach the mode at  $1238\mu\text{Hz}$  (807 s). This band has a width at least twice as wide as any other. What is different about this mode???

## 4.2. Mode Identification

GD358 is extensively studied (????). Our current work has produced a well defined sequence of modes. The previous identification of these modes as a series of  $l=1$  radial overtones is based mostly on the pulsation frequency distribution and limited spectroscopic analysis (??). It is important to further investigate these identifications as we initiate an indepth asteroseismic investigations.

GD358’s combination frequencies provide a tool by which we can bolster  $l$  identifications. Combination frequencies are typically observed in the FTs of moderate to large amplitude pulsators. They are identified by their exact numerical relationships with parent frequencies. The combinations themselves are not independent, but result from nonlinear effects associated with the surface convection zone (????). ? lays the groundwork, showing that observed amplitudes of the combination frequencies depend on geometric factors such as the  $(l, m)$  indices of the parents and the inclination of the pulsation axis to the line of sight.

The methods outlined in ? and ? work best when applied to larger amplitude frequencies detected in high signal to noise data sets such as provided by extensive WET runs. The primary reason for this is that combination frequencies are lower amplitude than their parents, and so are more difficult to detect in sparse data. We chose the 1990, 1994, 2006, 2010, 2011, and 2014 observing seasons, and looked at pulsation frequencies with amplitudes above 10 mma.

Figure ?? shows the resulting probability distribution of  $l$  and  $m$  values for the  $1735.96\mu\text{Hz}$  frequency detected in 2014.

Finally, given the  $l=1$  identification, but the lack of definite multiplet structure, the best way to determine the  $l=0$  component for each band is simply to average the frequencies in the bands. We experimented with numerous weighting techniques, and determined there is no significant difference in our solutions. Our final frequency identification for each band is given in Table ??.

## 5. Pulsational properties

## 6. Asteroseismic fitting

??

The basic method in our asteroseismic fitting consists of calculating grids of white dwarf models and running a fitting subroutine to match the periods of the models ( $P_{\text{calc}}$ ) with the observed periods and calculated residuals using the usual formula

$$\sigma_{\text{RMS}} = \sqrt{\frac{\sum_1^{n_{\text{obs}}} (P_{\text{calc}} - P_{\text{obs}})^2}{n_{\text{obs}}}}, \quad (1)$$

where  $n_{\text{obs}}$  is the number of periods present in the pulsation spectrum.

### 6.1. The Models

To compute our models, we used the White Dwarf Evolution Code (WDEC). The WDEC evolves hot polytrope models from temperatures above 100,000 K down to the temperature of our choice. Models in the temperature range of interest for the present study are thermally relaxed solutions to the stellar structure equations. Each model we compute for our grids is the result of such an evolutionary sequence. The WDEC is described in detail in ? and ?. We used smoother core composition profiles and implemented more complex profiles that result from stellar evolution calculations (?). We updated the envelope equation of state tables from those calculated by ? to those given by ?. We use OPAL opacities (?) and plasmon neutrino rates published by ?.

DBVs are younger than their cooler cousins the DAVs. Time-dependent diffusion calculations (e.g. ??) show that at 24,000 K, a typical temperature for a DBV, the carbon has not fully settled into the core of the star yet. We expect the helium layer to be separated into a mixed He/C layer with a pure He layer on top, as shown in Fig. 8. Following ?, we adopted and parameterized this structure in our models.

### 6.2. Initial grid search

In our asteroseismic fits, we initially varied six parameters; the effective temperature, the mass and four structure parameters. There are two parameters associated with the



shapes of the oxygen (and carbon) core composition profiles: the central oxygen abundance ( $X_o$ ) and the edge of the homogeneous carbon and oxygen core ( $q_{\text{fm}}$ , as a fraction of stellar mass. For envelope structure,  $M_{\text{env}}$  marks the location of the base of the helium layer and  $M_{\text{He}}$  the location where the helium abundance rises to 1 (see Figure 8).  $M_{\text{env}}$  and  $M_{\text{He}}$  are mass coordinates, defined as e.g.  $M_{\text{env}} = -\log(1 - M(r)/M_*)$ , where  $M(r)$  is the mass enclosed in radius  $r$  and  $M_*$  is the stellar mass.

We started with a master grid (table ??) chosen so that it covered all relevant area of parameter space and had sufficient resolution, based on previous experience (??) to find any region of local minimum in the fitness parameter, but was small enough to be computationally manageable. The master grid involved the computation of 10,483,200 models. We fit simultaneously all 15 periods, requiring all of them to be  $\ell = 1$  modes. The results of this initial fit are shown in the left panel of figure 9.

### 6.3. Asymptotic period spacing

Before we refine the period-by-period fitting optimization, it is worth stepping back and consider what we can learn from the average period spacing of GD358. The average period spacing provides a useful asteroseismic measure of the mass and temperature of the star, independent of the details of internal chemical composition profiles. Higher  $k$  modes are not strongly trapped in the core and according to asymptotic theory, they should be nearly evenly spaced in period. This spacing is given by (Unno et al. 1989)

$$\Delta P = \frac{\pi}{\ell(\ell + 1)^{1/2}} \left[ \int_{r_1}^{r_2} \frac{N}{r} dr \right]^{-1}, \quad (2)$$

where  $r_1$  and  $r_2$  are turning points of the mode and  $N$  is the Brunt-Väisälä frequency. The asymptotic period spacing is  $\ell$  dependent, with higher  $\ell$  modes having smaller spacing. In the case of GD 358, we have a single  $\ell = 1$  sequence so we only need to worry about the dependence of the asymptotic period spacing on the Brunt-Väisälä frequency. Much if not all of GD 358’s pulsation spectrum is in the asymptotic limit, because the shortest period observed is a  $k = 8$  mode.

The dependence of  $\Delta P$  on the Brunt-Väisälä frequency leads to higher mass and lower temperature models having a smaller period spacing (their interior is less compressible). This effect appears in asteroseismic fitting of white dwarfs and also sdB stars as a ubiquitous diagonal trend in contour maps of the quality of the fits in the mass-effective temperature plane (e.g. ???). One requirement for the periods of the model to match the observed

periods is that the average period spacing in the models matches the average period spacing in the observed pulsation spectrum. If a good match occurs for a given mass and effective temperature, then models with lower mass but higher effective temperature will also match well.

We can use the sequence of 13 consecutive  $\ell = 1$  modes we have with GD 358 to calibrate our models. Using the  $\ell = 1$  sequence of modes, we compute an average period spacing of 39.08 seconds. We call this  $\Delta P_{\text{obs}}$ . For each model in the master grid, we compute an asymptotic period spacing ( $\Delta P_{\text{calc}}$ ). This asymptotic period spacing is calculated by first discarding the first 10 modes. The exact value of 10 is somewhat arbitrary, but it is chosen so that the modes we use in our computation are indeed in the asymptotic limit. The higher  $k$  modes show weaker trapping than the lower  $k$  modes. We then fit a line through the set  $(k_i, P_i)$ . The slope gives us the asymptotic period spacing in the model. We also calculate the residuals of the fits and as an additional check, discard the models that have residuals above a certain limit. The limit is chosen by checking the procedure by eye on a few models.

We show a contour map of the location of the models that best match the average period spacing of 39.08 seconds in Fig. 8, right panel. We place it side by side with a contour map showing the location of the best fit model in the same region of parameter space, based on the master grid fitting described in section 6.2. Note how the best fit model falls right within the valley where the period spacings between GD358 and the models match. This should come as no surprise, as in order for 15 periods to fit reasonably well, the model period list should have a spacing similar to that of the observed period spectrum. It is also somewhat comforting to find that the spectroscopic data point also falls within the swath where the period spacings match (though the best fit model based on the master grid search is further down the valley).

One can fit simultaneously the average period spacing and the individual periods formally while performing the fits by using some prescription to calculate the fitness parameter Travis,canadians?. This leads to a more complex relation than defined in equation 1. Note that the period spacing is a much weaker constraint than the individual period fit. If one takes 4 seconds as an upper limit for fitness, that includes a single point in the period-by-period fit plot (left panel in Fig 9), but the entire parameter plane for the average period spacing fit plot (right panel). We bypass the difficulty of assigning proper weights to each constraint by taking the average period spacing fit into account as an initial step to refine our fits. We refine our fits by calculating models on a higher resolution grid that fall within the region defined by the two diagonal lines shown in the right panel of figure 9, then performing a period-by-period fit using equation 1.

#### 6.4. Determining the best grid resolution for refined fits

Having determined a more restricted region of parameter space to search for the best fit models, we now turn to the question of how fine we need to make our refined grid. We want to have a high enough resolution grid that we can be sure we captured a true minimum, but on the other hand, there are computational limitations to how many models we can afford to calculate, save, and process.

One way to gain a sense of how fine the grid needs to be is to make single parameter cuts through parameter space. Fig. 10 shows such a cut for master grid models. The plot was made by fixing 5 of the 6 parameters to their best fit value ( $M_* = 0.590M_\odot$ ,  $M_{\text{env}} = 2.40$ ,  $M_{\text{He}} = 5.15$ ,  $X_o = 0.45$ , and  $q_{\text{fm}} = 0.15$ ). We allowed the effective temperature to vary through the entire range considered for the master grid (table ??). One can see that the fits are generally poor, though they do seem to settle to a minimum in a smooth way. Except for the striking anomaly at 26,600 K. Upon further investigation, we discovered that anomaly to be due to a single period in the pulsation spectrum: the 968 s mode. In the model, that mode appears highly sensitive to some parameters, and in a non-continuous way.

This is unsettling, as it is easy to see that one might miss the best fit models if the grid is not fine enough. In order to quantify "fine enough", we ran systematic scans, computing models with 5 parameter fixed and allowing the 6th parameter to vary in very fine steps. We went all the way down in step sizes to  $\Delta T_{\text{eff}} = 1$  K,  $\Delta M_* = 0.1M_\odot$ ,  $\Delta M_{\text{env}} = \Delta M_{\text{He}} = 1$ ,  $\Delta X_o = 1$ , and  $\Delta q_{\text{fm}} = 0.1$ . Results for 4 different parameters are shown in Fig 11. The figure includes zooms to regions of interest. Other modes also exhibit a behavior similar to the 968 s mode, in different regions of parameter space. For instance, the jumps in  $\sigma_{\text{RMS}}$  for  $q_{\text{fm}}$  between 0.3 and 0.4 are due to sudden changes in the 854.5 and 902.5 s modes.

Regardless of the behavior of individual modes in the models as the parameters vary, we can assert from the test above what step sizes will allow us to minimize our risk of missing a minimum. We settled on optimal step sizes of  $\Delta T_{\text{eff}} = 20$ ,  $\Delta M_* = 0.2$ ,  $\Delta M_{\text{He}} = 20$ ,  $\Delta X_o = 20$ , and  $\Delta q_{\text{fm}} = 1$  for our refined grid. To offset the computational cost, we fixed  $M_{\text{env}}$  to a canonical value of 2.80 (?). It is clear from the second panel in Fig. 11 that there is only a weak dependence of the fits on that parameter.

## 7. Results of the period fitting

## 8. Discussion and Conclusions

Lessons learned: how fine a grid must be. CAUTION with pipeline fitting. we learn that one must exert extreme caution in any automated pipeline-type fitting of white dwarf stars. Asymptotic theory

We recover the trend in mass/teff plane

We confirm the weak dependence on 4 interior parameters.

We calibrated our models.

*Facilities:* MCAO:0.6m (), Struve(), KPNO:2.1m (), , BOAO:1.8m (), Lulin:1.8m (), Beijing:2.16m (), Maidanek:1.5m (), Peak Terskol

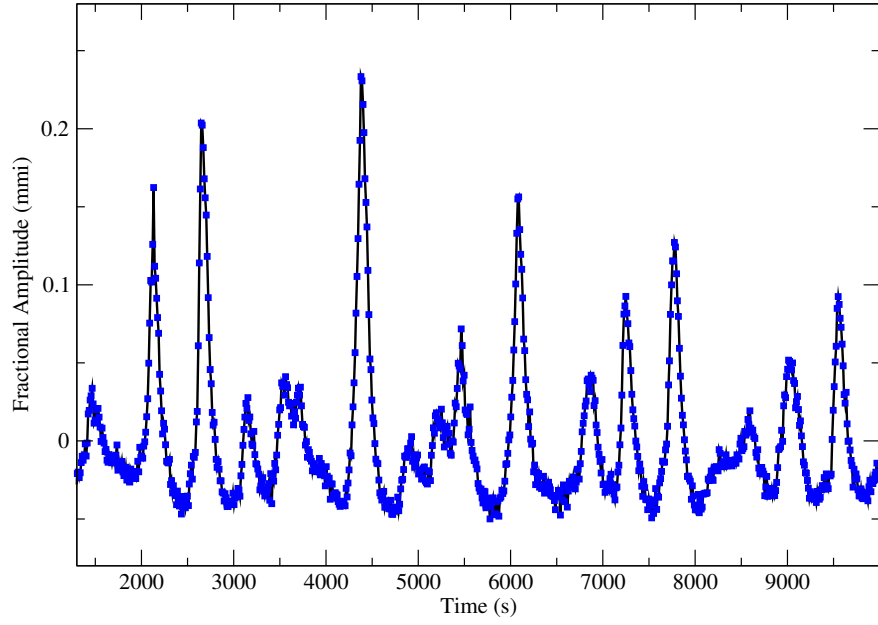


Fig. 1.— Light curve of GD358 obtained with the Peak Terskol 2.0m. Each point corresponds to a 10 s exposure. The nonlinear, multiperiodic nature of this star is clearly evident.

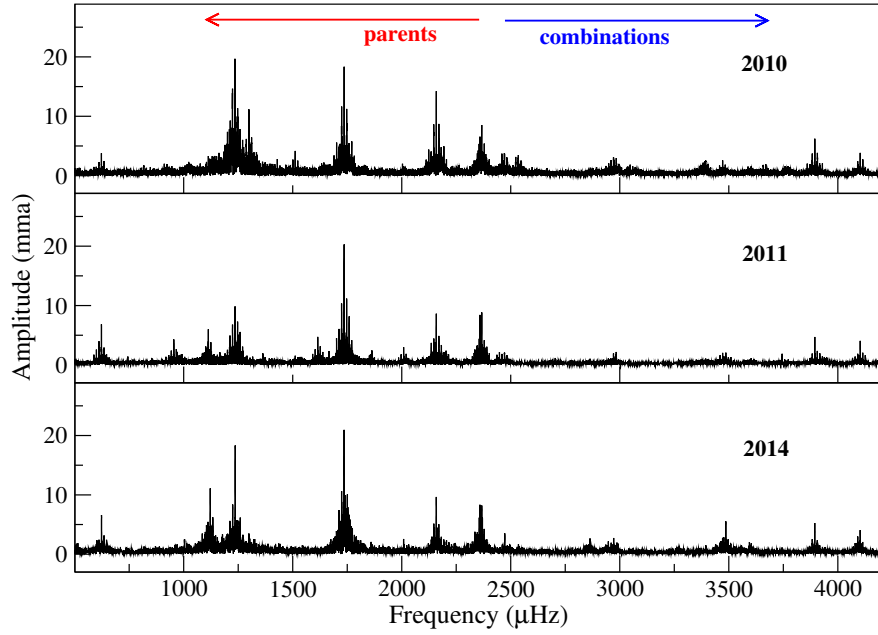


Fig. 2.— Fourier Transforms of GD358 for the 2010, 2011, and 2014 observing seasons. The frequency range of the observed series of  $\ell = 1$  modes discussed in Section 4 is indicated by the left arrow (red). Peaks below  $\approx 2400 \mu\text{Hz}$  are combination frequencies discussed in Section 4 (right arrow, blue). (A color version of this figure is available in the online journal.)

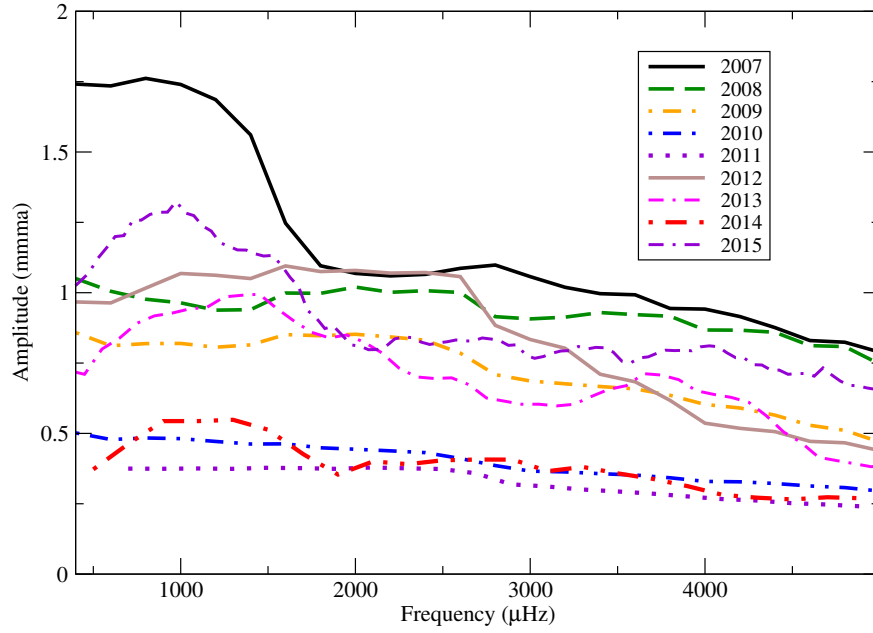


Fig. 3.— A comparison of the average noise as a function of frequency for the 2007-2015 observing seasons. Each data set was prewhitened by its dominant frequencies. The noise levels for each season are somewhat different. This must be taken into account during frequency analysis.

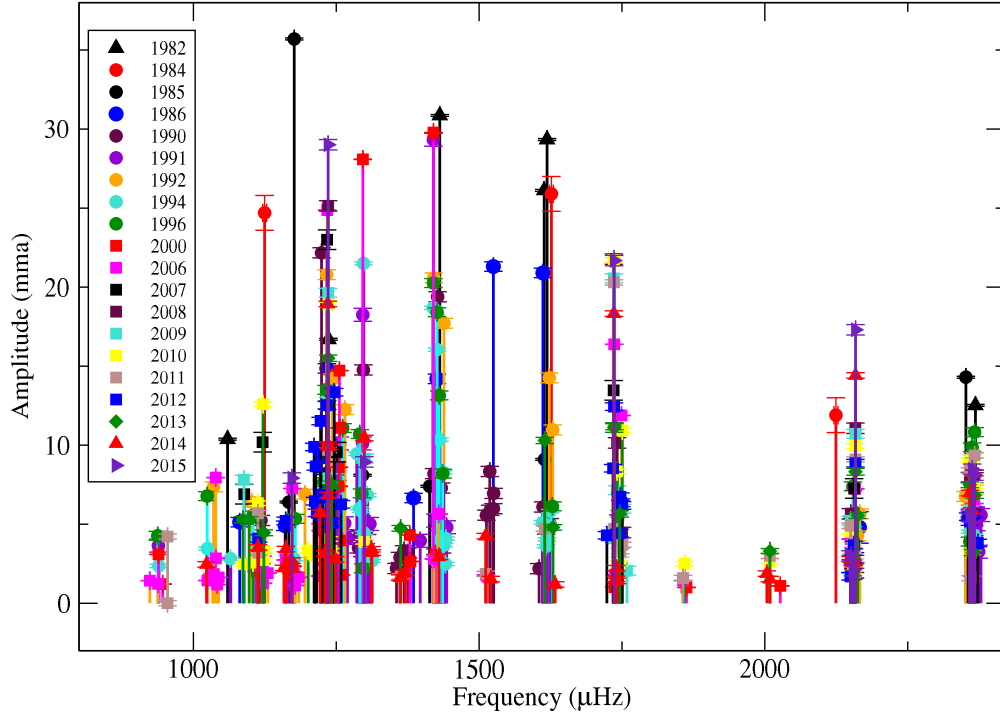


Fig. 4.— A schematic representation of GD358’s pulsation modes for all available data between 1982 and 2015. Systematic patterns of distribution are evident. The bands between 2400 and 1000  $\mu\text{Hz}$  (400 and 1000 s) are of particular importance for this work. (A color version of this figure is available in the online journal.)



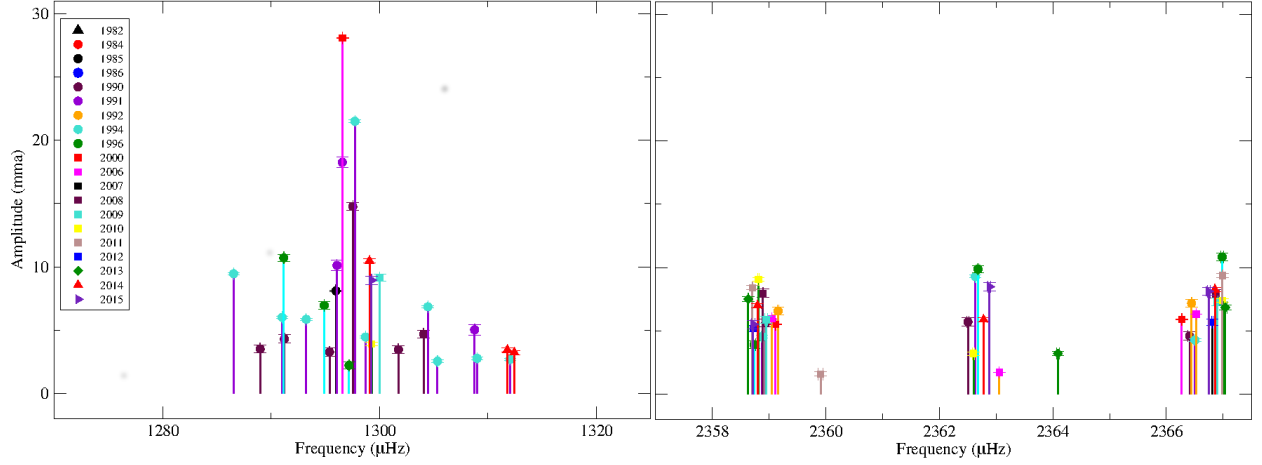


Fig. 5.— The detailed schematic distribution of frequencies for the bands near 1300 *right* and 2360  $\mu\text{Hz}$ *left*. The 1300  $\mu\text{Hz}$ band shows no multiplet structure, unlike the 2360  $\mu\text{Hz}$ band. Here we see clear evidence of multiplet structure. Assuming the triplet structure represents  $l = 1$ , this implies a rotation period of  $\approx 1.5$  days. Note changes in the scale for both axes. (A color version of this figure is available in the online journal.)

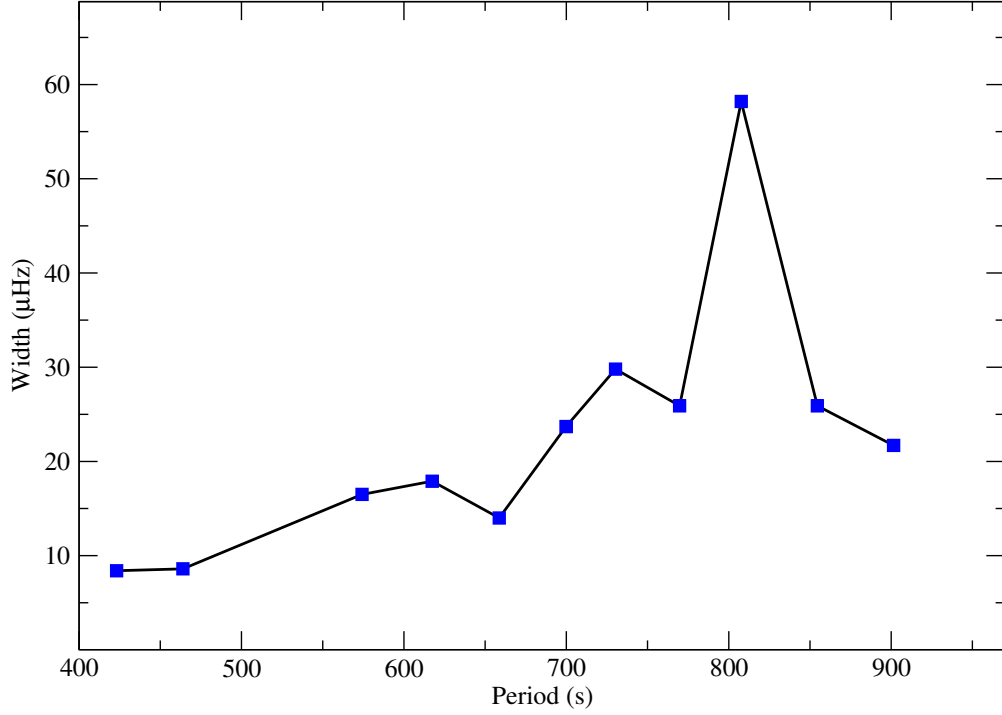


Fig. 6.— Width of each bank of power in Fig. 4. We find an overall increase in band thickness with decreasing frequency (increasing period). The band at 807 s has a width at least twice as large as other bands.

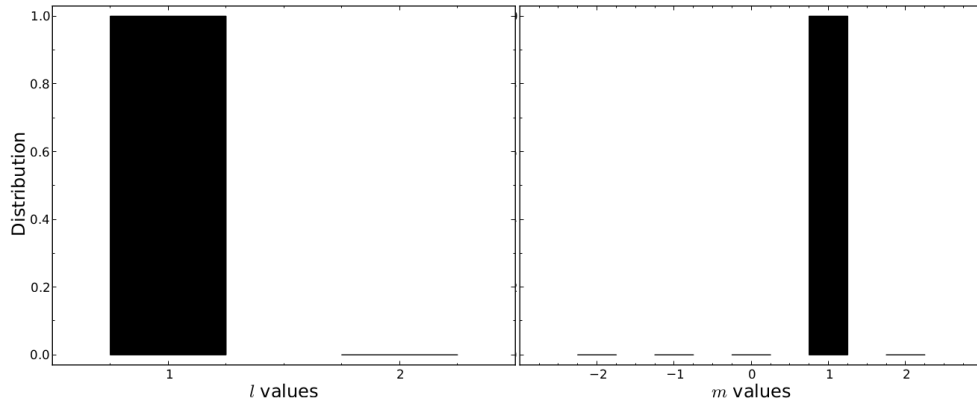


Fig. 7.— Probability distribution (from 0 to 1) of  $l$  and  $m$  values for the 1735.96 variation detected in 2014. The solutions are from individual simulations with  $Res_{rms} < 9.5e - 06$ . The amplitudes of the observed combination frequencies argue that this is  $l=1$ ,  $m=1$ .

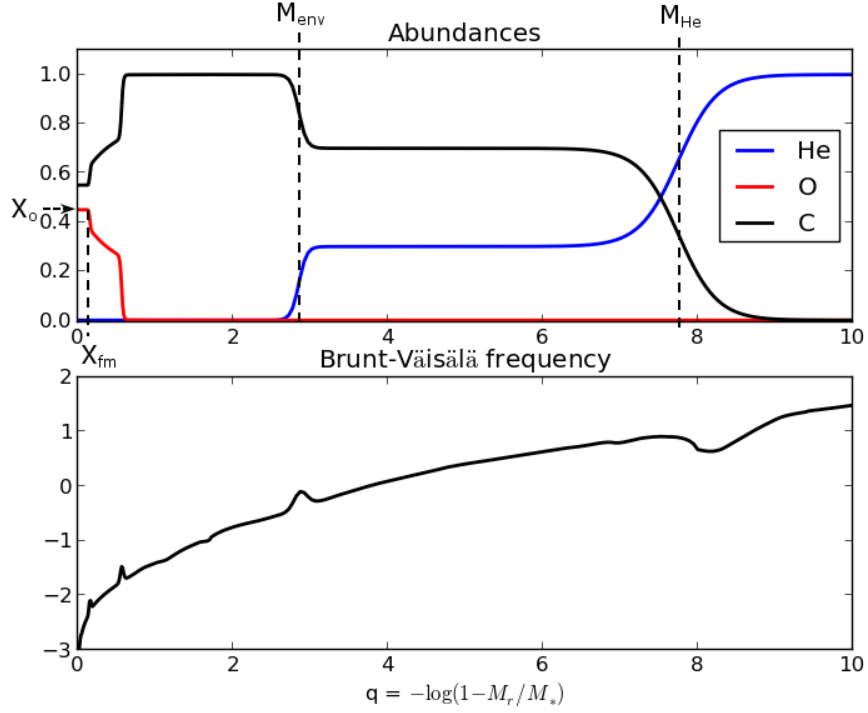


Fig. 8.— *Upper panel:* Chemical composition profiles of our models to illustrate the parameterization of the internal chemical structure. The center of the model is to the left and the surface to the right.  $q = 2$  corresponds to  $M_r = 0.99 M_*$ . The vertical axis shows fractional abundances. *Lower panel:* The corresponding Brunt-Väisälä frequency ( $\log N^2$  on the vertical axis). Each chemical transition leads to a bump in the Brunt-Väisälä frequency.

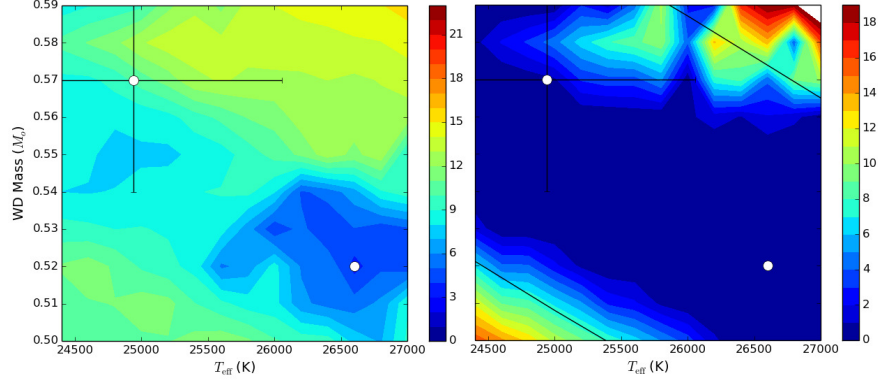


Fig. 9.— *Left panel:* Contour map showing the location of the best fit models. The quantity plotted in the mass-effective temperature plane is the fitness parameter defined in equation 1. The scale is in seconds. *Right panel:* Contour map of the difference between the average periods spacing determined from GD 358’s periods and the asymptotic period spacing of the models, in the mass-effective temperature plane. The scale is in 10s of seconds, so the worse matches pictured on the plot have  $|\Delta P_{\text{obs}} - \Delta P_{\text{calc}}| \sim 2$  s.

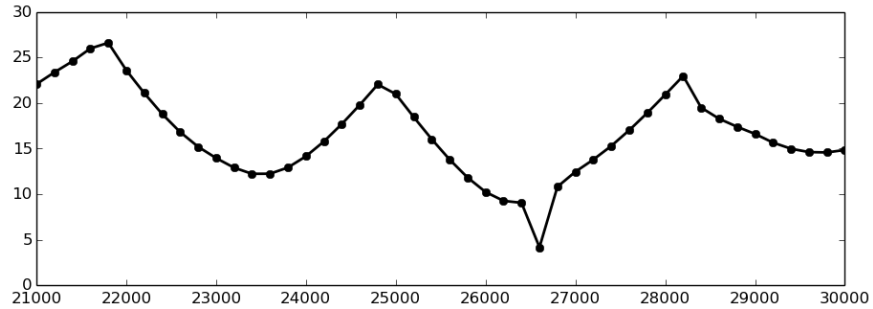


Fig. 10.— Dependence of the fitness parameter on effective temperature alone based on the master grid of models.

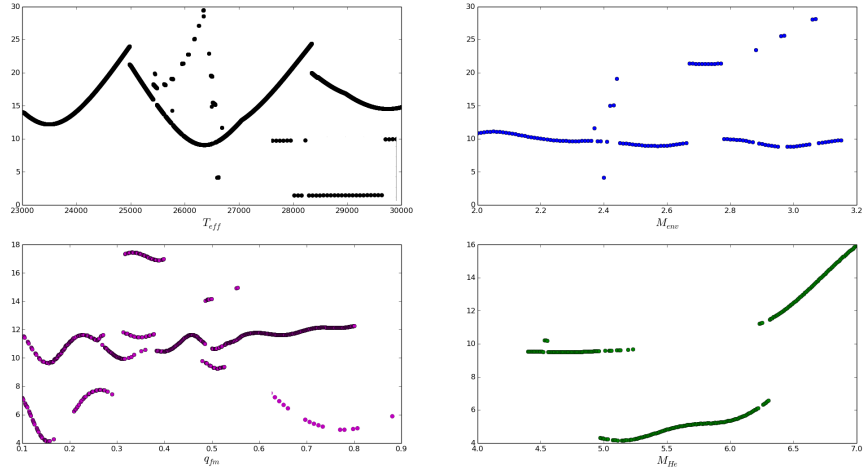


Fig. 11.— Dependence of the fitness parameter on different parameters. The 5 parameters not shown on the horizontal axis in each plot are held to fixed values corresponding to the best fit model.

Table 1.

Run Name	Telescope	Detector	Date	Length (hrs)
mcao070524-01	MCAO 0.6	CCD	2007-05-24	4.0
mcao070531-02	MCAO 0.6	CCD	2007-05-31	4.1
mcao080613-01	MCAO 0.6	CCD	2008-06-13	2.0
mcao080617-02	MCAO 0.6	CCD	2008-07-25	1.2
mcao080726-01	MCAO 0.6	CCD	2008-07-26	1.7
mcao080730-01	MCAO 0.6	CCD	2008-07-30	3.5
mcao080802-01	MCAO 0.6	CCD	2008-08-02	3.7
pjmo080706-03	PJMO 0.6	CCD	2008-07-06	5.1
suho080810-19	Suhora 0.6	CCD	2008-08-10	4.7
suho080811-19	Suhora 0.6	CCD	2008-08-11	2.5
boao090528-17	BOAO 1.8	CCD	2009-05-28	2.0
kore090529-16	BOAO 1.8	CCD	2009-05-29	2.4
mcao090513-01	MCAO 0.6	CCD	2009-05-13	2.4
mcao090519-03	MCAO 0.6	CCD	2009-05-19	3.2
mcao090520-01	MCAO 0.6	CCD	2009-05-20	4.8
mcao090521-01	MCAO 0.6	CCD	2009-05-21	4.9
mcao090522-01	MCAO 0.6	CCD	2009-05-22	3.1
mcao090531-02	MCAO 0.6	CCD	2009-05-31	2.1
mcao090601-01	MCAO 0.6	CCD	2009-06-01	3.3
mole090526-20	Moletai 1.65	CCD	2009-05-26	3.7
suho090520-19	Suhora 0.6	CCD	2009-05-20	2.2
suho090521-19	Suhora 0.6	CCD	2009-05-21	5.1
vien090525-19	Vienna 0.6	CCD	2009-05-25	6.2
krak100523-20	Krakow 0.4	CCD	2010-05-23	3.4
krak100526-20	Krakow 0.4	CCD	2010-05-26	2.3
krak100616-20	Krakow 0.4	CCD	2010-06-16	4.3
krak100617-20	Krakow 0.4	CCD	2010-06-17	4.5
mcao100516-01	MCAO 0.6	CCD	2010-05-16	2.0
mcao100521-01	MCAO 0.6	CCD	2010-05-21	0.9
mcao100521-05	MCAO 0.6	CCD	2010-05-21	0.8
mcao100526-01	MCAO 0.6	CCD	2010-05-26	3.3
mcdo100517-06	McDonald 2.1	CCD	2010-05-17	4.8
mole100516-22	Moletai 1.65	CCD	2010-05-26	1.8
mole100517-22	Moletai 1.65	CCD	2010-05-17	2.0
mole100520-21	Moletai 1.65	CCD	2010-05-20	3.3
mole100521-21	Moletai 1.65	CCD	2010-05-21	3.5

Table 1—Continued

Run Name	Telescope	Detector	Date	Length (hrs)
pjmo100519-04	PJMO 0.6	CCD	2010-05-19	4.0
pjmo100520-02	PJMO 0.6	CCD	2010-05-20	3.8
pjmo100521-05	PJMO 0.6	CCD	2010-05-21	3.3
pjmo100522-02	PJMO 0.6	CCD	2010-05-22	7.0
pjmo100523-04	PJMO 0.6	CCD	2010-05-23	6.0
pjmo100524-02	PJMO 0.6	CCD	2010-05-24	7.5
pjmo100527-02	PJMO 0.6	CCD	2010-05-27	8.3
pjmo100528-02	PJMO 0.6	CCD	2010-05-28	8.3
pjmo100619-03	PJMO 0.6	CCD	2010-06-19	4.0
pjmo100622-02	PJMO 0.6	CCD	2010-06-22	0.7
suho100617-21	Suhora 0.6	CCD	2010-06-17	4.3
terb100516-17	Terskol 2.0	CCD	2010-05-16	2.4
terb100520-17	Terskol 2.0	CCD	2010-05-20	8.9
terb100521-20	Terskol 2.0	CCD	2010-05-21	4.0
terb100524-19	Terskol 2.0	CCD	2010-05-24	5.6
terb100525-17	Terskol 2.0	CCD	2010-05-25	7.3
tueb100522-20	Tuebingen 0.8	SBig	2010-05-22	5.9
tueb100523-20	Tuebingen 0.8	SBig	2010-05-23	5.9
tueb100524-20	Tuebingen 0.8	SBig	2010-05-24	6.0
tueb100604-20	Tuebingen 0.8	SBig	2010-06-04	5.8
tueb100605-20	Tuebingen 0.8	SBig	2010-06-05	5.3
turk100512-18	Canakkale 1.2	CCD	2010-05-12	6.6
turk100513-22	Canakkale 1.2	CCD	2010-05-13	2.8
turk100516-19	Canakkale 1.2	CCD	2010-05-16	6.4
turk100520-19	Canakkale 1.2	CCD	2010-05-20	1.1
turk100522-21	Canakkale 1.2	CCD	2010-05-22	2.6
turk100523-19	Canakkale 1.2	CCD	2010-05-23	6.0
turk100611-19	Canakkale 1.2	CCD	2010-06-11	5.2
turk100613-19	Canakkale 1.2	CCD	2010-06-13	5.3
turk100615-20	Canakkale 1.2	CCD	2010-06-15	4.8
turk100618-19	Canakkale 1.2	CCD	2010-06-18	4.5
turk100620-20	Canakkale 1.2	CCD	2010-06-20	4.8
hvar110521-22	Hvar 1.0	CCD	2011-05-21	2.6
hvar110526-19	Hvar 1.0	CCD	2011-05-26	6.6
hvar110527-19	Hvar 1.0	CCD	2011-05-27	3.5
hvar110529-19	Hvar 1.0	CCD	2011-05-29	6.7
hvar110531-19	Hvar 1.0	CCD	2011-05-31	4.3
hvar110602-19	Hvar 1.0	CCD	2011-06-02	3.8
hvar110604-19	Hvar 1.0	CCD	2011-06-04	6.6
hvar110606-20	Hvar 1.0	CCD	2011-06-06	4.4

Table 1—Continued

Run Name	Telescope	Detector	Date	Length (hrs)
krak110506-20	Krakow 0.4	CCD	2011-05-06	5.4
krak110509-19	Krakow 0.4	CCD	2011-05-09	6.7
krak110510-19	Krakow 0.4	CCD	2011-05-10	6.2
krak110511-19	Krakow 0.4	CCD	2011-05-11	6.7
krak110512-19	Krakow 0.4	CCD	2011-05-12	3.1
krak110516-19	Krakow 0.4	CCD	2011-05-16	6.1
krak110517-19	Krakow 0.4	CCD	2011-05-17	5.6
krak110518-19	Krakow 0.4	CCD	2011-05-18	5.7
krak110519-20	Krakow 0.4	CCD	2011-05-19	5.4
krak110520-20	Krakow 0.4	CCD	2011-05-20	5.2
krak110522-21	Krakow 0.4	CCD	2011-05-22	4.3
krak110523-23	Krakow 0.4	CCD	2011-05-23	1.4
krak110524-19	Krakow 0.4	CCD	2011-05-24	4.0
krak110525-20	Krakow 0.4	CCD	2011-05-25	5.4
krak110526-20	Krakow 0.4	CCD	2011-05-26	5.3
krak110529-20	Krakow 0.4	CCD	2011-05-29	5.0
krak110530-20	Krakow 0.4	CCD	2011-05-30	4.8
krak110531-20	Krakow 0.4	CCD	2011-05-31	0.8
krak110604-20	Krakow 0.4	CCD	2011-06-04	5.3
mole110426-22	Moletai 1.65	CCD	2011-04-26	1.7
mole110427-21	Moletai 1.65	CCD	2011-04-27	3.7
mole110430-20	Moletai 1.65	CCD	2011-04-30	0.8
mole110502-20	Moletai 1.65	CCD	2011-05-02	0.4
mole110502-21	Moletai 1.65	CCD	2011-05-02	2.6
mole110505-20	Moletai 1.65	CCD	2011-05-05	1.1
mole110510-21	Moletai 1.65	CCD	2011-05-10	3.5
mtlm110426-05	Mt. Lemmon 1.0	CCD	2011-04-26	6.3
mtlm110427-06	Mt. Lemmon 1.0	CCD	2011-04-27	5.5
mtlm110428-04	Mt. Lemmon 1.0	CCD	2011-04-28	7.1
mtlm110429-05	Mt. Lemmon 1.0	CCD	2011-04-29	6.8
mtlm110430-05	Mt. Lemmon 1.0	CCD	2011-04-30	6.4
mtlm110501-05	Mt. Lemmon 1.0	CCD	2011-05-01	6.6
mtlm110502-05	Mt. Lemmon 1.0	CCD	2011-05-02	6.5
naoc110426-13	NAOC 0.5	CCD	2011-04-26	6.9
naoc110427-11	NAOC 0.5	CCD	2011-04-27	3.3



Table 1—Continued

Run Name	Telescope	Detector	Date	Length (hrs)
naos110426-13	NAOC 0.85	CCD	2011-04-26	6.9
naos110427-11	NAOC 0.85	CCD	2011-04-27	3.3
naos110428-12	NAOC 0.85	CCD	2011-04-28	2.6
naos110501-13	NAOC 0.85	CCD	2011-05-01	7.1
naos110502-12	NAOC 0.85	CCD	2011-05-02	8.3
naos110505-13	NAOC 0.85	CCD	2011-05-05	7.0
pjmo110426-07	PJMO 0.6	CCD	2011-04-26	3.0
pjmo110428-04	PJMO 0.6	CCD	2011-04-28	2.0
pjmo110429-03	PJMO 0.6	CCD	2011-04-29	2.5
pjmo110430-04	PJMO 0.6	CCD	2011-04-30	3.0
pjmo110503-04	PJMO 0.6	CCD	2011-05-03	2.6
pjmo110518-03	PJMO 0.6	CCD	2011-05-18	6.7
pjmo110519-03	PJMO 0.6	CCD	2011-05-19	2.7
pjmo110521-03	PJMO 0.6	CCD	2011-05-21	2.7
pjmo110524-02	PJMO 0.6	CCD	2011-05-24	5.2
pjmo110525-07	PJMO 0.6	CCD	2011-05-25	3.2
pjmo110526-03	PJMO 0.6	CCD	2011-05-26	7.0
pjmo110527-02	PJMO 0.6	CCD	2011-05-27	0.8
pjmo110527-03	PJMO 0.6	CCD	2011-05-27	6.7
suho110521-20	Suhora 0.6	CCD	2011-05-21	5.2
suho110522-19	Suhora 0.6	CCD	2011-05-22	5.9
suho110523-20	Suhora 0.6	CCD	2011-05-23	5.6
suho110527-20	Suhora 0.6	CCD	2011-05-27	2.0
suho110529-20	Suhora 0.6	CCD	2011-05-29	4.6
suho110530-20	Suhora 0.6	CCD	2011-05-30	4.9
terb110527-20	Terskol 2.0	CCD	2011-05-27	2.4
terb110529-17	Terskol 2.0	CCD	2011-05-27	4.4
terb110530-18	Terskol 2.0	CCD	2011-05-30	2.6
terb110531-17	Terskol 2.0	CCD	2011-05-31	1.8
terb110601-19	Terskol 2.0	CCD	2011-06-01	3.3

Table 1—Continued

Run Name	Telescope	Detector	Date	Length (hrs)
tueb110504-19	Tuebingen 0.8	SBig	2011-05-04	6.8
tueb110505-19	Tuebingen 0.8	SBig	2011-05-05	6.8
tueb110506-19	Tuebingen 0.8	SBig	2011-05-06	6.7
tueb110508-19	Tuebingen 0.8	SBig	2011-05-08	6.6
tueb110509-19	Tuebingen 0.8	SBig	2011-05-09	6.7
tueb110513-19	Tuebingen 0.8	SBig	2011-05-13	2.2
tueb110518-22	Tuebingen 0.8	SBig	2011-05-18	4.1
tueb110523-20	Tuebingen 0.8	SBig	2011-05-23	5.9
tueb110524-20	Tuebingen 0.8	SBig	2011-05-24	5.9
tueb110525-20	Tuebingen 0.8	SBig	2011-05-24	6.0
tueb110529-20	Tuebingen 0.8	SBig	2011-05-29	5.9
tueb110530-20	Tuebingen 0.8	SBig	2011-05-30	3.4
tubi110602-00	Tubitak 1.0	CCD	2011-06-02	1.1
tubi110602-23	Tubitak 1.0	CCD	2011-06-02	2.0
tubi110603-20	Tubitak 1.0	CCD	2011-06-03	5.2
boao120418-18	BOAO 1.8	CCD	2012-04-18	1.7
krak120418-00	Krakow 0.4	CCD	2012-04-18	1.8
krak120421-00	Krakow 0.4	CCD	2012-04-21	4.6
krak120423-00	Krakow 0.4	CCD	2012-04-23	1.7
krak120428-00	Krakow 0.4	CCD	2012-04-28	6.6
krak120429-00	Krakow 0.4	CCD	2012-04-29	6.1
krak120430-00	Krakow 0.4	CCD	2012-04-30	6.7
mtlm120419-10	Mt. Lemmon 1.0	CCD	2012-04-19	1.7
mtlm120420-10	Mt. Lemmon 1.0	CCD	2012-04-20	1.4
mtlm120421-05	Mt. Lemmon 1.0	CCD	2012-04-21	6.2
mtlm120422-07	Mt. Lemmon 1.0	CCD	2012-04-22	4.8
na50120524-12	NAOC 0.5	CCD	2012-05-24	4.5
na50120525-12	NAOC 0.5	CCD	2012-05-25	4.4
na50120526-14	NAOC 0.5	CCD	2012-05-26	3.3
na50120527-12	NAOC 0.5	CCD	2012-05-27	4.9
na50120530-13	NAOC 0.5	CCD	2012-05-30	6.0

Table 1—Continued

Run Name	Telescope	Detector	Date	Length (hrs)
pjmo120425-03	PJMO 0.6	CCD	2012-04-25	7.2
pjmo120426-03	PJMO 0.6	CCD	2012-04-26	4.3
prom120430-04	PROMPT 0.4	CCD	2012-04-30	2.2
prom120430-07	PROMPT 0.4	CCD	2012-04-30	1.1
prom120501-04	PROMPT 0.4	CCD	2012-05-01	4.5
prom120502-04	PROMPT 0.4	CCD	2012-05-02	4.4
prom120503-04	PROMPT 0.4	CCD	2012-05-03	0.9
prom120504-04	PROMPT 0.4	CCD	2012-05-04	4.5
prom120509-04	PROMPT 0.4	CCD	2012-05-09	4.3
prom120510-04	PROMPT 0.4	CCD	2012-05-10	4.1
prom120511-03	PROMPT 0.4	CCD	2012-05-11	4.1
prom120512-03	PROMPT 0.4	CCD	2012-05-12	4.0
prom120513-03	PROMPT 0.4	CCD	2012-05-13	2.1
prom120514-03	PROMPT 0.4	CCD	2012-05-14	4.0
prom120515-03	PROMPT 0.4	CCD	2012-05-15	4.0
suho120501-20	Suhora 0.6	CCD	2012-05-01	6.0
suho120502-21	Suhora 0.6	CCD	2012-05-02	5.1
suho120503-23	Suhora 0.6	CCD	2012-05-03	2.4
suho120505-19	Suhora 0.6	CCD	2012-05-05	2.1
tubi120420-01	Tubitak 1.0	CCD	2012-04-20	1.0
tubi120423-19	Tubitak 1.0	CCD	2012-04-23	6.6
tubi120512-20	Tubitak 1.0	CCD	2012-04-23	5.2
caam130412-21	Cannakkale 1.2	CCD	2013-04-12	4.0
caam130417-21	Cannakkale 1.2	CCD	2013-04-17	3.2
caam130418-21	Cannakkale 1.2	CCD	2013-04-18	4.5
krak130418-00	Krakow 0.4	CCD	2013-04-18	6.7
krak130421-00	Krakow 0.4	CCD	2013-04-18	7.4
krak130425-00	Krakow 0.4	CCD	2013-04-25	6.7
krak130426-00	Krakow 0.4	CCD	2013-04-26	2.1
naos130503-13	NAOC 0.85	CCD	2013-05-03	6.0
pjmo130429-06	PJMO 0.6	CCD	2013-04-29	2.7
pjmo130430-07	PJMO 0.6	CCD	2013-04-30	2.1
pjmo130503-07	PJMO 0.6	CCD	2013-05-03	3.6
pjmo130505-04	PJMO 0.6	CCD	2013-05-05	6.8
suho130422-21	Suhora 0.6	CCD	2013-04-22	4.6
suho130425-20	Suhora 0.6	CCD	2013-04-25	5.9
suho130426-20	Suhora 0.6	CCD	2013-04-26	5.4
suho130501-19	Suhora 0.6	CCD	2013-05-01	6.1
suho130504-21	Suhora 0.6	CCD	2013-05-04	4.4
suho130505-19	Suhora 0.6	CCD	2013-05-05	5.5

Table 1—Continued

Run Name	Telescope	Detector	Date	Length (hrs)
caam140610-19	Cannakkale 1.2	CCD	2014-06-10	5.5
krak140530-21	Krakow 0.4	CCD	2014-05-30	2.4
krak140604-20	Krakow 0.4	CCD	2014-06-04	5.5
krak140606-20	Krakow 0.4	CCD	2014-06-06	4.7
krak140607-20	Krakow 0.4	CCD	2014-06-07	5.1
krak140608-20	Krakow 0.4	CCD	2014-06-08	5.2
krak140609-19	Krakow 0.4	CCD	2014-06-09	4.7
krak140610-20	Krakow 0.4	CCD	2014-06-10	2.4
mcao140602-05	MCAO 0.6	CCD	2014-06-02	3.0
mcao140603-01	MCAO 0.6	CCD	2014-06-03	4.1
mcao140607-01	MCAO 0.6	CCD	2014-06-07	4.0
mcao140608-01	MCAO 0.6	CCD	2014-06-08	3.9
mole140526-20	Moletai 1.65	CCD	2014-05-26	2.5
mole140527-20	Moletai 1.65	CCD	2014-05-27	3.7
mole140605-20	Moletai 1.65	CCD	2014-06-05	3.3
mole140607-20	Moletai 1.65	CCD	2014-06-07	2.9
naos140605-15	NAOC 0.85	CCD	2014-06-05	5.7
naos140606-17	NAOC 0.85	CCD	2014-06-06	3.9
pjmo140519-04	PJMO 0.6	CCD	2014-05-19	4.0
pjmo140529-03	PJMO 0.6	CCD	2014-05-29	5.4
pjmo140530-03	PJMO 0.6	CCD	2014-05-30	4.3
pjmo140531-02	PJMO 0.6	CCD	2014-05-31	5.0
pjmo140601-03	PJMO 0.6	CCD	2014-06-01	3.3
pjmo140602-02	PJMO 0.6	CCD	2014-06-02	4.5
pjmo140603-02	PJMO 0.6	CCD	2014-06-03	7.1
pjmo140604-04	PJMO 0.6	CCD	2014-06-04	5.8
pjmo140611-03	PJMO 0.6	CCD	2014-06-11	5.9
suho140604-19	Suhora 0.6	CCD	2014-06-04	4.4
suho140606-20	Suhora 0.6	CCD	2014-06-06	4.7
ters140604-20	Terskol 0.6	CCD	2014-06-04	2.0
ters140619-20	Terskol 0.6	CCD	2014-06-19	6.0

Table 1—Continued

Run Name	Telescope	Detector	Date	Length (hrs)
tsao140524-17	Tien Shan 1.0	CCD	2014-05-24	4.7
tsao140525-16	Tien Shan 1.0	CCD	2014-05-25	6.0
tsao140610-15	Tien Shan 1.0	CCD	2014-06-10	1.0
tsao140611-16	Tien Shan 1.0	CCD	2014-06-11	6.0
tsao140613-17	Tien Shan 1.0	CCD	2014-06-13	4.6
tsao140616-19	Tien Shan 1.0	CCD	2014-06-16	1.4
tsao140619-17	Tien Shan 1.0	CCD	2014-06-19	4.8
tsao140620-18	Tien Shan 1.0	CCD	2014-06-20	3.1
tsao140627-16	Tien Shan 1.0	CCD	2014-06-27	5.9
tsao140628-16	Tien Shan 1.0	CCD	2014-06-28	5.9
krak150420-20	Krakow 0.4	CCD	2015-05-20	2.1
krak150421-19	Krakow 0.4	CCD	2015-05-21	7.5
pjmo150420-03	PJMO 0.6	CCD	2015-04-20	7.3
pjmo150421-05	PJMO 0.6	CCD	2015-04-21	5.4
pjmo150422-03	PJMO 0.6	CCD	2015-04-22	4.7
pjmo150426-03	PJMO 0.6	CCD	2015-04-26	7.4
prom150428-08	PROMPT 0.4	CCD	2015-04-28	6.5
prom150429-03	PROMPT 0.6	CCD	2015-04-29	6.6
prom150501-03	PROMPT 0.6	CCD	2015-05-01	6.2

Table 2. 1982-2006 Detected Independent Frequencies

Frequency $\mu\text{Hz}$	Period s	Amplitude mma	Signal/Noise
1982			
$1236.483 \pm 0.07$	808.75	$16.70 \pm 0.06$	9.4
$1431.112 \pm 0.04$	698.76	$30.86 \pm 0.06$	11.4
$1613.842 \pm 0.05$	619.65	$26.12 \pm 0.06$	9.7
$1618.845 \pm 0.06$	617.72	$29.34 \pm 0.06$	10.9
$2368.563 \pm 0.10$	422.20	$12.52 \pm 0.06$	5.8
1984			
$1124.701 \pm 3.5$	889.13	$24.7 \pm 1.1$	7.2
$1626.474 \pm 3.5$	614.83	$25.9 \pm 1.1$	6.8
1985			
$1166.944 \pm 0.05$	856.94	$6.43 \pm 0.06$	11
$1176.489 \pm 0.03$	849.99	$35.70 \pm 0.06$	16.0
$1614.554 \pm 0.04$	619.37	$9.15 \pm 0.06$	4.6
$2351.762 \pm 0.04$	425.22	$14.34 \pm 0.06$	12
1986			
$1081.025 \pm 0.03$	925.05	$5.1 \pm 0.4$	4.6
$1160.678 \pm 0.03$	861.57	$4.9 \pm 0.4$	4.5
$1223.803 \pm 0.02$	817.12	$9.3 \pm 0.4$	9.1
$1233.585 \pm 0.01$	810.65	$14.9 \pm 0.4$	14.5
$1385.240 \pm 0.03$	721.90	$6.7 \pm 0.4$	6.4
$1426.181 \pm 0.01$	701.17	$14.2 \pm 0.4$	14.3
$1525.030 \pm 0.01$	655.72	$21.3 \pm 0.4$	21.4
$1611.691 \pm 0.01$	620.47	$20.9 \pm 0.4$	20.9
$2157.783 \pm 0.04$	463.44	$2.4 \pm 0.4$	4
$2165.564 \pm 0.03$	461.77	$4.8 \pm 0.4$	4
$2368.938 \pm 0.03$	422.13	$5.8 \pm 0.4$	5.6

Table 2—Continued

Frequency $\mu\text{Hz}$	Period s	Amplitude mma	Signal/Noise
1990			
1112.933 $\pm$ 0.03	898.53	2.31 $\pm$ 0.32	4.0
1114.180 $\pm$ 0.03	897.52	2.44 $\pm$ 0.32	4.1
1118.324 $\pm$ 0.02	894.20	5.24 $\pm$ 0.32	8.9
1119.089 $\pm$ 0.03	893.58	2.83 $\pm$ 0.32	4.8
1224.216 $\pm$ 0.03	816.83	22.17 $\pm$ 0.32	4.0
1233.413 $\pm$ 0.03	810.76	4.80 $\pm$ 0.32	8.4
1245.395 $\pm$ 0.03	802.96	2.17 $\pm$ 0.32	4.0
1288.995 $\pm$ 0.03	775.80	3.50 $\pm$ 0.32	6.3
1291.229 $\pm$ 0.03	774.46	4.31 $\pm$ 0.32	7.6
1295.400 $\pm$ 0.03	771.96	3.27 $\pm$ 0.32	5.8
1297.540 $\pm$ 0.01	770.69	14.76 $\pm$ 0.32	26.1
1304.075 $\pm$ 0.03	766.83	4.67 $\pm$ 0.32	8.3
1355.447 $\pm$ 0.03	737.76	2.20 $\pm$ 0.32	4.0
1361.728 $\pm$ 0.03	734.36	2.90 $\pm$ 0.32	5.2
1368.588 $\pm$ 0.03	730.68	3.32 $\pm$ 0.32	5.9
1375.434 $\pm$ 0.03	727.04	3.18 $\pm$ 0.32	5.7
1421.041 $\pm$ 0.02	703.71	8.22 $\pm$ 0.32	15.1
1423.704 $\pm$ 0.03	702.39	3.11 $\pm$ 0.32	5.8
1427.365 $\pm$ 0.01	700.59	19.39 $\pm$ 0.32	35.8
1428.663 $\pm$ 0.03	699.96	2.61 $\pm$ 0.32	4.8
1433.729 $\pm$ 0.02	697.48	7.29 $\pm$ 0.32	13.5
1435.209 $\pm$ 0.03	696.76	3.50 $\pm$ 0.32	6.5
1512.798 $\pm$ 0.02	661.03	5.57 $\pm$ 0.32	10.7
1518.661 $\pm$ 0.02	658.47	8.34 $\pm$ 0.32	15.9
1519.372 $\pm$ 0.02	658.17	5.88 $\pm$ 0.32	11.2
1524.924 $\pm$ 0.02	655.77	5.98 $\pm$ 0.32	11.2
1525.498 $\pm$ 0.02	655.52	6.95 $\pm$ 0.32	13.0
1611.741 $\pm$ 0.02	620.45	6.09 $\pm$ 0.32	12.3
1617.380 $\pm$ 0.03	618.28	4.69 $\pm$ 0.32	9.7
1623.709 $\pm$ 0.02	615.87	5.04 $\pm$ 0.32	10.2
2154.009 $\pm$ 0.03	464.25	4.40 $\pm$ 0.32	11.2
2157.765 $\pm$ 0.03	463.44	2.27 $\pm$ 0.32	5.8
2358.946 $\pm$ 0.02	423.92	5.63 $\pm$ 0.32	14.1
2362.507 $\pm$ 0.02	423.28	5.71 $\pm$ 0.32	14.3
2366.408 $\pm$ 0.03	422.58	4.59 $\pm$ 0.32	11.5

Table 2—Continued

Frequency $\mu\text{Hz}$	Period s	Amplitude mma	Signal/Noise
1991			
$1296.087 \pm 0.13$	771.55	$10.11 \pm 0.41$	17.7
$1296.577 \pm 0.13$	771.26	$18.25 \pm 0.41$	29.8
$1308.777 \pm 0.05$	764.07	$5.02 \pm 0.41$	9.9
$1396.945 \pm 0.05$	715.85	$3.95 \pm 0.41$	8.4
$1419.934 \pm 0.01$	704.26	$29.3 \pm 0.41$	45.6
$1423.333 \pm 0.04$	702.58	$5.23 \pm 0.41$	6.3
$1427.062 \pm 0.04$	700.74	$5.02 \pm 0.41$	7.4
$1443.381 \pm 0.05$	692.82	$4.81 \pm 0.41$	9.7
$2150.307 \pm 0.05$	465.05	$2.36 \pm 0.41$	4.1
$2154.389 \pm 0.05$	464.17	$2.79 \pm 0.41$	4.6
$2157.939 \pm 0.05$	463.41	$2.62 \pm 0.41$	4.4
$2370.121 \pm 0.04$	421.92	$5.01 \pm 0.41$	9.2
$2374.211 \pm 0.05$	421.19	$3.26 \pm 0.41$	5.7
$2378.195 \pm 0.04$	420.49	$5.58 \pm 0.41$	10.7
1992			
$1035.357 \pm 0.05$	965.85	$7.35 \pm 0.31$	4.1
$1101.952 \pm 0.05$	907.48	$6.40 \pm 0.31$	3.7
$1195.349 \pm 0.003$	836.58	$6.90 \pm 0.31$	4.1
$1233.263 \pm 0.001$	810.86	$20.79 \pm 0.31$	13.5
$1242.854 \pm 0.003$	804.60	$14.20 \pm 0.31$	8.8
$1265.279 \pm 0.003$	790.34	$12.25 \pm 0.31$	7.1
$1420.845 \pm 0.001$	703.81	$20.59 \pm 0.31$	13.1
$1438.411 \pm 0.003$	695.21	$17.71 \pm 0.31$	11.9
$1622.795 \pm 0.003$	616.22	$14.26 \pm 0.31$	9.2
$1628.812 \pm 0.004$	613.94	$10.9 \pm 0.317$	6.5
$2162.104 \pm 0.007$	462.51	$4.26 \pm 0.31$	4.2
$2166.094 \pm 0.007$	461.66	$5.66 \pm 0.31$	4.8
$2351.041 \pm 0.007$	425.34	$6.75 \pm 0.31$	5.2
$2359.162 \pm 0.007$	423.88	$6.55 \pm 0.31$	9.2
$2366.443 \pm 0.007$	422.58	$7.17 \pm 0.31$	6.3



Table 2—Continued

Frequency $\mu\text{Hz}$	Period s	Amplitude mma	Signal/Noise
1994			
$939.264 \pm 0.007$	1064.66	$2.36 \pm 0.10$	5.7
$1024.773 \pm 0.011$	975.83	$3.46 \pm 0.10$	8.8
$1064.931 \pm 0.012$	939.03	$2.82 \pm 0.10$	7.4
$1106.833 \pm 0.013$	903.48	$2.56 \pm 0.10$	7.0
$1113.548 \pm 0.012$	898.03	$3.95 \pm 0.10$	9.4
$1164.637 \pm 0.012$	858.64	$3.12 \pm 0.10$	8.6
$1176.684 \pm 0.013$	849.85	$2.79 \pm 0.10$	7.2
$1224.306 \pm 0.012$	816.79	$3.28 \pm 0.10$	9.1
$1234.488 \pm 0.013$	810.05	$2.70 \pm 0.10$	7.7
$1235.491 \pm 0.005$	809.39	$13.13 \pm 0.10$	37.3
$1242.357 \pm 0.013$	804.92	$3.33 \pm 0.10$	9.1
$1246.494 \pm 0.013$	802.25	$2.69 \pm 0.10$	7.8
$1286.550 \pm 0.003$	777.27	$9.45 \pm 0.10$	27.6
$1291.023 \pm 0.009$	774.58	$6.07 \pm 0.10$	17.8
$1293.244 \pm 0.009$	773.25	$5.85 \pm 0.10$	16.1
$1297.737 \pm 0.005$	770.57	$21.5 \pm 0.10$	61.9
$1298.710 \pm 0.010$	769.99	$4.45 \pm 0.10$	12.5
$1304.464 \pm 0.009$	766.64	$6.84 \pm 0.10$	19.9
$1305.352 \pm 0.013$	766.08	$2.54 \pm 0.10$	7.0
$1309.003 \pm 0.013$	763.94	$2.76 \pm 0.10$	8.4
$1312.045 \pm 0.013$	762.17	$2.67 \pm 0.10$	7.9
$1419.641 \pm 0.003$	704.40	$18.70 \pm 0.10$	54.4
$1422.947 \pm 0.013$	702.77	$2.86 \pm 0.10$	8.2
$1426.395 \pm 0.003$	701.07	$16.05 \pm 0.10$	46.6
$1430.851 \pm 0.005$	698.88	$10.35 \pm 0.10$	30.1
$1433.167 \pm 0.010$	697.75	$4.06 \pm 0.10$	11.6
$1437.607 \pm 0.006$	695.60	$8.28 \pm 0.10$	24.1
$1438.523 \pm 0.011$	695.16	$3.68 \pm 0.10$	10.7
$1440.997 \pm 0.012$	693.96	$2.48 \pm 0.10$	7.2
$1441.910 \pm 0.009$	693.52	$4.09 \pm 0.10$	11.9
$1611.351 \pm 0.009$	620.60	$5.12 \pm 0.10$	14.2
$1617.450 \pm 0.010$	618.26	$3.61 \pm 0.10$	9.5
$1618.545 \pm 0.009$	617.84	$4.04 \pm 0.10$	11.2
$1624.624 \pm 0.009$	615.53	$5.83 \pm 0.10$	16.1
$1625.634 \pm 0.009$	615.14	$4.89 \pm 0.10$	13.9

Table 2—Continued

Frequency $\mu\text{Hz}$	Period s	Amplitude mma	Signal/Noise
$2150.498 \pm 0.010$	465.01	$3.22 \pm 0.10$	9.4
$2154.130 \pm 0.010$	464.22	$4.75 \pm 0.10$	13.7
$2157.844 \pm 0.012$	463.43	$2.70 \pm 0.10$	7.6
$2358.880 \pm 0.010$	423.93	$4.53 \pm 0.10$	13.5
$2362.636 \pm 0.005$	423.26	$9.29 \pm 0.10$	31.2
$2366.505 \pm 0.011$	422.56	$4.26 \pm 0.10$	13.2
1996			
$937.695 \pm 0.028$	1066.44	$4.27 \pm 0.28$	3.5
$1024.276 \pm 0.028$	976.30	$6.78 \pm 0.28$	6.4
$1104.483 \pm 0.025$	905.40	$5.55 \pm 0.28$	5.1
$1178.461 \pm 0.025$	848.56	$5.34 \pm 0.28$	5.5
$1227.936 \pm 0.022$	814.37	$7.66 \pm 0.28$	7.5
$1233.14 \pm 0.015$	810.94	$13.50 \pm 0.28$	12.1
$1234.506 \pm 0.015$	810.04	$12.53 \pm 0.28$	11.2
$1247.959 \pm 0.022$	801.31	$7.84 \pm 0.28$	4.1
$1261.275 \pm 0.015$	792.85	$11.08 \pm 0.28$	11.6
$1291.169 \pm 0.015$	774.49	$10.71 \pm 0.28$	9.7
$1294.899 \pm 0.025$	772.26	$6.95 \pm 0.28$	7.9
$1297.194 \pm 0.010$	770.89	$22.05 \pm 0.28$	2.4
$1420.057 \pm 0.010$	704.20	$20.26 \pm 0.28$	19.7
$1426.443 \pm 0.010$	701.04	$18.41 \pm 0.28$	8.3
$1430.253 \pm 0.012$	699.18	$13.15 \pm 0.28$	12.8
$1436.261 \pm 0.022$	696.25	$8.20 \pm 0.28$	9.1
$1628.296 \pm 0.028$	614.14	$6.13 \pm 0.28$	6.3
$2154.117 \pm 0.028$	464.23	$7.40 \pm 0.28$	7.1
$2358.806 \pm 0.025$	423.94	$6.01 \pm 0.28$	4.7
$2362.617 \pm 0.014$	423.26	$9.87 \pm 0.28$	9.0
$2367.288 \pm 0.025$	422.42	$8.92 \pm 0.28$	11.6

Table 2—Continued

Frequency $\mu\text{Hz}$	Period s	Amplitude mma	Signal/Noise
2000			
$938.991 \pm 0.015$	1064.95	$3.09 \pm 0.01$	9.4
$946.238 \pm 0.015$	1056.82	$1.20 \pm 0.01$	4.0
$1110.999 \pm 0.015$	900.09	$1.98 \pm 0.01$	7.0
$1171.564 \pm 0.015$	853.56	$1.89 \pm 0.01$	7.0
$1173.021 \pm 0.012$	852.50	$2.32 \pm 0.01$	8.8
$1251.851 \pm 0.004$	798.82	$3.21 \pm 0.01$	12.5
$1254.503 \pm 0.002$	797.13	$8.60 \pm 0.01$	33.1
$1255.583 \pm 0.002$	796.44	$14.72 \pm 0.01$	67.1
$1256.248 \pm 0.005$	796.02	$8.04 \pm 0.01$	42.6
$1257.268 \pm 0.010$	795.38	$3.05 \pm 0.01$	15.2
$1258.288 \pm 0.010$	794.73	$2.06 \pm 0.01$	5.7
$1296.603 \pm 0.001$	771.25	$28.08 \pm 0.01$	109.5
$1378.795 \pm 0.008$	725.27	$4.33 \pm 0.01$	17.3
$1379.737 \pm 0.010$	724.78	$2.64 \pm 0.01$	10.4
$1420.101 \pm 0.001$	704.18	$29.78 \pm 0.01$	118.8
$1423.597 \pm 0.010$	702.45	$3.08 \pm 0.01$	12.3
$1736.660 \pm 0.014$	575.82	$1.02 \pm 0.01$	4.0
$2150.515 \pm 0.013$	465.01	$2.99 \pm 0.01$	11.2
$2154.040 \pm 0.013$	464.24	$5.38 \pm 0.01$	19.9
$2157.736 \pm 0.012$	463.45	$2.51 \pm 0.01$	9.5
$2359.118 \pm 0.008$	423.89	$5.51 \pm 0.01$	23.7
$2366.271 \pm 0.010$	422.61	$5.90 \pm 0.01$	25.1
2006			
$923.976 \pm 0.001$	1082.28	$1.43 \pm 0.01$	5.2
$938.216 \pm 0.002$	1065.85	$1.23 \pm 0.01$	4.4
$1024.496 \pm 0.002$	976.09	$1.44 \pm 0.01$	4.8
$1033.760 \pm 0.002$	967.34	$1.85 \pm 0.01$	6.9
$1039.075 \pm 0.001$	962.39	$7.95 \pm 0.01$	27.2
$1039.474 \pm 0.001$	962.02	$2.84 \pm 0.01$	9.7
$1041.535 \pm 0.001$	960.12	$1.18 \pm 0.01$	4.3
$1044.381 \pm 0.002$	957.50	$1.63 \pm 0.01$	6.2

Table 2—Continued

Frequency $\mu\text{Hz}$	Period s	Amplitude mma	Signal/Noise
$1113.582 \pm 0.001$	898.02	$2.71 \pm 0.01$	9.4
$1120.404 \pm 0.001$	892.53	$2.09 \pm 0.01$	7.3
$1120.902 \pm 0.001$	892.14	$2.98 \pm 0.01$	10.2
$1121.704 \pm 0.002$	891.50	$1.26 \pm 0.01$	4.4
$1130.144 \pm 0.002$	884.84	$1.91 \pm 0.01$	7.3
$1161.552 \pm 0.001$	860.92	$2.74 \pm 0.01$	9.6
$1173.015 \pm 0.001$	852.50	$7.26 \pm 0.01$	25.4
$1178.096 \pm 0.002$	848.83	$1.13 \pm 0.01$	4.3
$1184.470 \pm 0.002$	844.26	$1.64 \pm 0.01$	6.2
$1222.199 \pm 0.002$	818.20	$1.72 \pm 0.01$	6.3
$1222.751 \pm 0.001$	817.83	$5.04 \pm 0.01$	18.3
$1222.945 \pm 0.001$	817.70	$4.59 \pm 0.01$	5.1
$1228.185 \pm 0.002$	814.21	$2.71 \pm 0.01$	9.4
$1228.791 \pm 0.001$	813.81	$5.27 \pm 0.01$	19.0
$1234.124 \pm 0.001$	810.29	$24.87 \pm 0.01$	88.0
$1239.510 \pm 0.001$	806.77	$5.07 \pm 0.01$	18.3
$1240.237 \pm 0.002$	806.30	$2.85 \pm 0.01$	9.9
$1244.790 \pm 0.002$	803.35	$1.90 \pm 0.01$	6.9
$1245.219 \pm 0.001$	803.07	$4.75 \pm 0.01$	17.1
$1246.032 \pm 0.001$	802.55	$4.44 \pm 0.01$	15.2
$1421.012 \pm 0.002$	703.72	$2.81 \pm 0.01$	7.1
$1429.209 \pm 0.001$	699.69	$5.65 \pm 0.01$	22.5
$1512.141 \pm 0.002$	661.31	$1.79 \pm 0.01$	6.4
$1736.301 \pm 0.001$	575.94	$16.38 \pm 0.01$	75.2
$1737.962 \pm 0.002$	575.39	$1.80 \pm 0.01$	7.6
$1741.666 \pm 0.001$	574.16	$11.01 \pm 0.01$	49.7
$1743.733 \pm 0.001$	573.48	$5.59 \pm 0.01$	8.4
$1749.083 \pm 0.001$	571.73	$11.88 \pm 0.01$	50.2
$1856.845 \pm 0.002$	538.55	$1.44 \pm 0.01$	6.4
$2150.393 \pm 0.001$	465.03	$4.06 \pm 0.01$	17.3
$2154.223 \pm 0.001$	464.20	$5.50 \pm 0.01$	21.8
$2158.073 \pm 0.001$	463.38	$7.24 \pm 0.01$	29.0
$2359.052 \pm 0.001$	423.90	$5.94 \pm 0.01$	22.1
$2363.058 \pm 0.002$	423.18	$1.7 \pm 0.011$	6.0
$2366.524 \pm 0.001$	422.56	$6.31 \pm 0.01$	23.0

Table 3. 2007-2015 Detected Independent Frequencies

Frequency $\mu\text{Hz}$	Period s	Amplitude mma	Signal/Noise
2007			
$1088.951 \pm 0.05$	918.31	$6.9 \pm 0.7$	5
$1121.169 \pm 0.04$	891.93	$10.19 \pm 0.7$	8
$1233.956 \pm 0.02$	810.40	$23 \pm 0.7$	20
$1251.1930.05$	799.24	$9.56 \pm 0.7$	8
$1735.4440.03$	576.22	$13.47 \pm 0.7$	13
$2156.2880.03$	463.76	$7.26 \pm 0.7$	7
2008			
$1235.745 \pm 0.004$	809.23	$25.14 \pm 0.33$	23.9
$1735.716 \pm 0.004$	576.13	$21.77 \pm 0.33$	22.6
$1741.459 \pm 0.009$	574.23	$10.14 \pm 0.33$	9.8
$1750.185 \pm 0.012$	571.37	$4.47 \pm 0.33$	5.6
$2150.245 \pm 0.011$	465.06	$5.66 \pm 0.33$	7.7
$2158.416 \pm 0.01$	463.30	$11.07 \pm 0.33$	11
$2358.895 \pm 0.01$	423.93	$7.95 \pm 0.33$	10.2
$2366.872 \pm 0.01$	422.50	$7.93 \pm 0.33$	10.2
2009			
$1088.445 \pm 0.018$	918.74	$7.82 \pm 0.28$	9
$1235.845 \pm 0.007$	809.16	$9.64 \pm 0.28$	22.4
$1236.849 \pm 0.018$	808.51	$7.91 \pm 0.28$	9.1
$1300.029 \pm 0.018$	576.29	$4.10 \pm 0.28$	4.7
$1735.699 \pm 0.006$	576.14	$20.60 \pm 0.28$	22.8
$1741.415 \pm 0.018$	574.25	$7.15 \pm 0.28$	8.8
$1750.525 \pm 0.012$	571.26	$5.98 \pm 0.28$	6.8
$2150.261 \pm 0.014$	465.06	$5.22 \pm 0.28$	6.5
$2158.474 \pm 0.003$	463.29	$10.72 \pm 0.28$	13.4
$2358.952 \pm 0.026$	423.92	$5.89 \pm 0.28$	8.1
$2366.893 \pm 0.018$	422.49	$7.28 \pm 0.28$	10.1
2010			
$1087.790 \pm 0.024$	919.29	$2.47 \pm 0.15$	5.1
$1104.397 \pm 0.023$	891.34	$2.57 \pm 0.15$	5.1
$1112.868 \pm 0.009$	898.58	$6.22 \pm 0.15$	13.2
$1121.9010.005$	891.34	$12.6 \pm 0.15$	26.6
$1122.674 \pm 0.021$	889.89	$2.73 \pm 0.15$	5.2
$1123.731 \pm 0.020$	891.33	$3.31 \pm 0.15$	7.1
$1200.999 \pm 0.017$	832.64	$3.33 \pm 0.15$	7.1
$1211.906 \pm 0.021$	825.15	$2.99 \pm 0.15$	6.4
$1236.278 \pm 0.003$	808.88	$18.9m0.15$	39.7

Table 4. List of 15 Periods Used in GD358 Fit.

$k$ ( $\mu\text{Hz}$ )	Frequency (s)	Period ( $\mu\text{Hz}$ )	Uncertainty (s)
8	2363.318	423.13	0.04
9	2155.544	463.92	0.04
10	2007.628	497.83	0.2
11	1857.716	538.30	0.3
12	1741.505	574.22	0.1
13	1619.700	617.40	0.2
14	1518.160	658.69	0.5
15	1428.943	699.82	0.2
16	1369.336	730.28	0.8
17	1299.147	769.74	0.2
18	1238.129	807.67	0.2
19	1170.207	854.55	0.6
20	1109.271	901.49	0.8
22	1032.967	968.09	1.4
24	941.333	1062.32	3.1

Table 5. Parameter Grid )

	$T_{\text{eff}}$ (K)	Mass $M_{\odot}$	$M_{\text{env}}$ $\log(M_*)$	$M_{\text{He}}$ $\log(M_*)$	$X_o$ $\log(M_*)$	$q_{\text{fm}}$ $\log(M_*)$
Minimum	21,000	0.500	2.00	4.00	0.10	0.10
Maximum	26,000	0.700	3.40	7.00	1.00	0.80
Step size	200	0.010	0.20	0.20	0.10	0.05